Dual-Frequency Phase Unwrapping for 3D InISAR Imaging of Non-Cooperative Targets

Francesco Mancuso, *Graduate Student Member, IEEE*, Elisa Giusti, *Senior Member, IEEE*, Brian Ng, *Member, IEEE*, and Marco Martorella, *Fellow, IEEE*

***Abstract*— The Three-Dimensional Interferometric Inverse Synthetic Aperture Radar Imaging (3D InISAR) method tackles the interpretability challenges associated with two-dimensional ISAR. It achieves this by providing a 3D representation of the target, offering a more comprehensive understanding of its shape and features. However, this approach faces challenges related to interferometric measurement ambiguity, especially in operational scenarios where factors such as target type and range of the target come into play. Conventional methods for interferogram unwrapping used in Interferometric SAR systems for topographic mapping cannot be directly applied to man-made objects in ISAR due to the discrete nature of ISAR imaging, which violates the assumption of spatial continuity. To address these issues, various multi-receiver solutions have been proposed in the literature. This paper introduces a different approach: a maximum likelihood-based dual-frequency technique applied to 3D InISAR imaging. Leveraging the frequency diversity inherent in a wideband receiver and utilizing two non-overlapping sub-bandwidths, this method effectively resolves measurement ambiguity. Testing the method in a simulated scenarios highlights the enhanced reconstruction abilities of the method and the benefits of utilizing extended physical baselines.**

***Index Terms*— Interferometry, ISAR, dual-frequency, 3D imaging, 3D InISAR, phase unwrapping, phase ambiguity, automatic target recognition.**

I. Introduction

THREE-DIMENSIONAL InISAR has been shown to be very effective in terms of three-dimensional reconstruction capabilities [1]. The primary objective of acquiring a three-dimensional reconstruction of a target is to enable accurate identification. The use of 2D ISAR images for the Automatic Target Recognition (ATR) task presents challenges due to the lack of information about the Image Projection Plane (IPP) [2]. However, with a 3D reconstruction of the target the IPP issue can be overcome, improving the classification process. Recently, researchers have proposed different approaches to address the three-dimensional target classification task [3], encompassing both classical model-based techniques [4], [5] and neural networks [6], [7].

Despite the advancements provided by this imaging technique, there is still a problem to be addressed. The reconstruction procedure is based on the assumption that the interferometric phase measurements are unambiguous (i.e., there is no phase wrapping), because phase differences that are integer multiples of 2π cannot be distinguished. In general, the measured interferometic phase $\theta_m(p)$ of the p-th pixel:

$$\theta_m(p) = \theta(p) + k(p) \cdot 2\pi \tag{1}$$

where $\theta(p) \in (-\pi, \pi]$ is the real interferometric phase of the p-th pixel and $k(p) \in \mathbb{Z}$ is the ambiguity number of the p-th pixel. The 3D InISAR technique utilises vertical and horizontal baselines arranged in an "L" shape. The occurrence of phase wrapping along these baselines impacts the quality of the final target reconstruction. The phase ambiguity depends on three factors: the operating wavelength of the system, the maximum target dimension (at any aspect) and its distance from the radar [8]. While the system's wavelength can be properly adjusted during design, the other two parameters remain unpredictable. Typically, the system is designed to function within a specific range of target sizes by selecting suitable antenna baselines [9], which can be a limit in operational scenarios. It is important to highlight that as the length of the baselines increases, height estimation accuracy improves [10]:

$$\sigma_h = \frac{\lambda R}{2\pi d} \cdot \sigma_\phi \,, \tag{2}$$

where σ_h is the standard deviation of the height estimation, λ is the operating wavelength of the system, R is the radar-target distance, d is the baseline length and σ_ϕ is the measured phase accuracy. Therefore, employing longer baselines would be advantageous for the system, provided phase ambiguity is avoided. In order to enhance the surveillance capability of the system, it is necessary to actively tackle the phase wrapping problem. Recently the dual orthogonal baselines 3D InISAR approach has also been used within a flying drones swarm [11] to image maritime targets [12]. In that specific

Manuscript received 27 September 2023; revised 13 December 2023, 14 February 2024, and 3 April 2024; accepted 6 April 2024. Date of publication 22 April 2024; date of current version 29 April 2024. This work was supported by the Office of Naval Research Global (ONR Global) titled "Automatic Target Recognition (ATR) by Means of Polarimetric Inverse Synthetic Aperture Radar (ISAR) Images and Multi-View Three Dimensional (3D) Interferometric Inverse Synthetic Aperture Radar (InISAR)" under Grant N62909-20-1-2062. *(Corresponding author: Francesco Mancuso.)*

Francesco Mancuso is with the Department of Information Engineering, University of Pisa, 56122 Pisa, Italy, and also with the Radar and Surveillance Systems (RaSS) National Laboratory of CNIT, 56124 Pisa, Italy (e-mail: francesco.mancuso@phd.unipi.it).

Elisa Giusti is with the Radar and Surveillance Systems (RaSS) National Laboratory of CNIT, 56124 Pisa, Italy (e-mail: elisa.giusti@cnit.it).

Brian Ng is with the School of Electrical and Mechanical Engineering, The University of Adelaide, Adelaide, SA 5005, Australia (e-mail: brian.ng@adelaide.edu.au).

Marco Martorella is with the Department of Electronic, Electrical and Systems Engineering, University of Birmingham, B15 2TT Birmingham, U.K., and also with the Radar and Surveillance Systems (RaSS) National Laboratory of CNIT, 56124 Pisa, Italy (e-mail: marco.martorella@cnit.it).

Digital Object Identifier 10.1109/TRS.2024.3392073

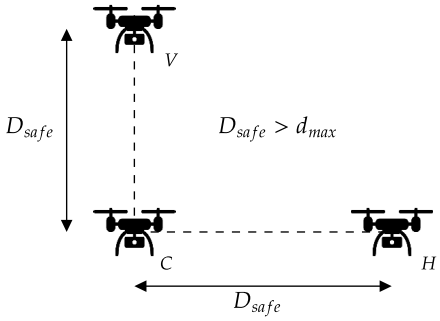

Fig. 1. Drone-based 3D InISAR configuration. D_{safe} is the minimum safe distance that must be kept among the drones, while d_{max} is the maximum unambiguous baselines size. Drone C is a TX/RX, while drones H and V are RX only.

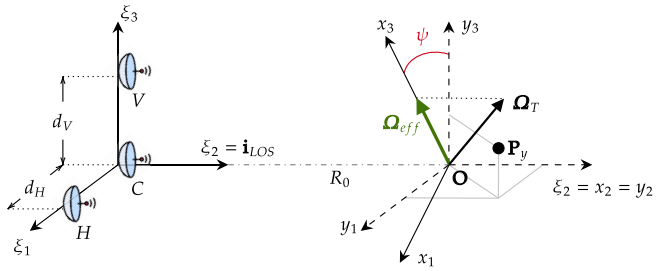

Fig. 2. Geometry of the radar-target system.

scenario the possibility to use longer baselines without having phase wrapping problems would be extremely useful, since the drones must keep a certain distance when flying in formation (Fig. 1) for safety reasons. This minumum distance could be greater than the maximum unambigous baselines length, leading to inaccurate three-dimensional reconstruction of the targets.

The problem of phase unwrapping in the Interferometric Syntetic Aperture Radar (InSAR) systems is well-known in literature [13], since InSAR is powerful technique for the monitoring of many important geophysical parameters [14], [15] (e.g., surface height, ground deformation, land cover characterisation). Due to its ill-posed nature, the single baseline phase unwrapping problem depends on the phase continuity assumption in order to determine a unique solution. Usually, it is assumed that any two neighboring pixels have an absolute phase difference not greater than π; this may be not true, for example, for high-frequency and large baseline systems, or when the SAR system is illuminating steep mountainous terrain. In the Interferometric ISAR, since we are imaging non-cooperative man-made object, the hypotheses of phase continuity does not apply due to the point-like structures in the image. This poses a significant limitation since conventional single baseline methods cannot be applied in such cases. One way to overcome the continuity requirement, is to use multi-baseline or multi-frequency systems [16] to obtain a well-posed problem. The first category uses multiple physical baselines in order to exploit the spatial diversity to measure different interferometric phase values and disambiguate the measurements. The main drawback of this approach is that the system would require a receiver for each new antenna, and each receveir chain would require a precise timing distribution, leading to an increment of costs and complexity. The second approach moves the burden in the frequency domain, by utilizing a single baseline and dividing the spectrum in two [17], [18], [19] or more sub-bandwidths [20]. This system could work with a single-receiver and a bank of pass-band filters, but obviously a wide overall bandwith would be necessary in order to keep the range resolution reasonable for the application, since the range resolution is given by the frequency span of the single sub-bandwidth.

To the authors knowledge, the phase unwrapping for a dual-baseline 3D InISAR system has been addressed only once by Wang and Chen [21] by exploiting a gradient-based approach [22]. There is another work about phase unwrapping for 3D InISAR by Yuan et al. [23], and it works by determining a bound for the ambiguity number, but it is applied to a bistatic geometry. The focus of this paper is the analysis of the applicability of the multi-frequency techniques to the 3D InISAR, to overcome the phase continuity hypothesis, and eventually enhance the surveillance capabilities of the system. The research aims to determine its suitability for the system and comprehensively understand its advantages and possible limitations. The proposed technique will be validated using a point-like simulated target, while an electromagnetically simulated target will be used to understand how the bandwidth splitting affects the result. These validation experiments are intended to assess the accuracy and effectiveness of the method, providing a comprehensive evaluation of its performance.

The paper is organized as follows. In Section II the system model and the geometry are introduced, followed by the multi-baseline and multi-frequency systems essentials. The Section III presents the Maximum Likelihood (ML) estimation approach for the phase unwrapping from the statistical model of the phase measurements, to the specific application in InISAR imaging. The results obtained by using the point-like boat are shown in Section IV. Finally, conclusions will be drawn in Section V.

II. System Model

The interferometric system consists of two baselines, positioned in the azimuth and elevation directions, respectively d_H and d_V, and equipped with three receivers, C, V and H. The central antenna C works also as a transmitter. The antennas are situated on a plane that is perpendicular to the Line-Of-Sight (LOS), which represents the straight line connecting the centers of the antennas and the target. It is assumed that the target is located in the far-field region. The diagram illustrating the system's geometry can be found in Fig. 2.

The phase center of the antenna array is located at the origin of the reference system T_ξ, which is integrated within the radar system. The LOS is aligned with with ξ_2 and the distance between the radar and the target is denoted as R_0. $\boldsymbol{\Omega}_T(t)$ denotes the angular rotation vector applied to the target's center O. The projection of $\boldsymbol{\Omega}_T(t)$ onto the plane perpendicular to the LOS determines the effective rotation vector, $\boldsymbol{\Omega}_{eff}(t)$. The Image Projection Plane (IPP) is the plane perpendicular to $\boldsymbol{\Omega}_{eff}(t)$. In order to obtain the three-dimensional reconstruction of the target, the modulus

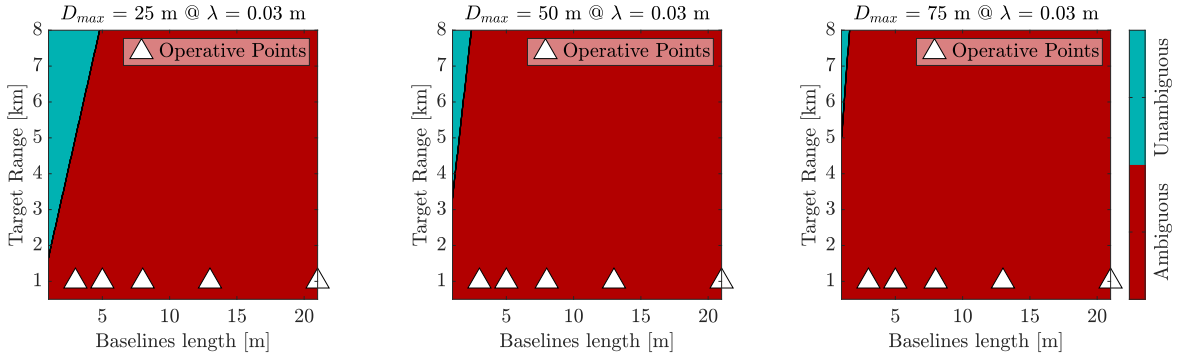

Fig. 3. Ambiguity regions of the system for a three different maximum target sizes at 10 GHz. The charts show five different operative points that represent five different baseline lengths and a target range of 1 km.

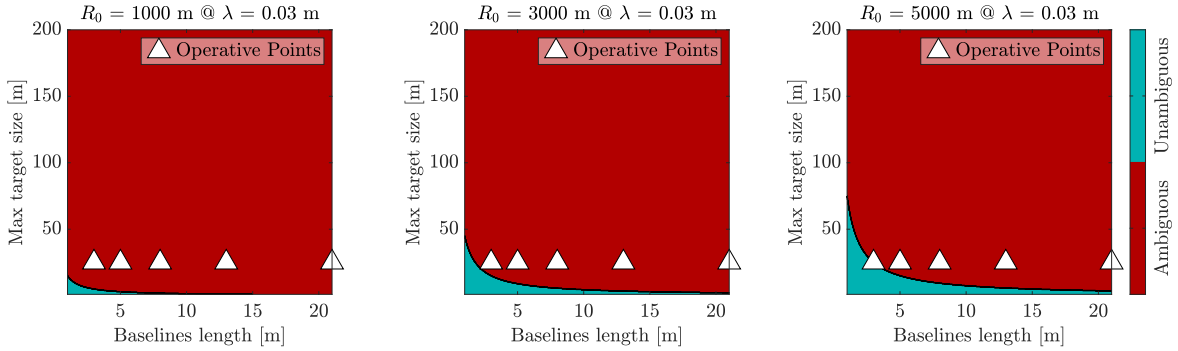

Fig. 4. Ambiguity regions of the system for a three different target ranges at 10 GHz. The charts show five different operative points that represent five different baseline lengths and target maximum size of 25 meters.

$\Omega_{eff} = \|\mathbf{\Omega}_{eff}\|$ (it is assumed that during the integration time T_{int} the vector $\mathbf{\Omega}_{eff}(t)$ is not varying, so the index t is dropped) and its direction ψ must be estimated. By using the relation that exist between the doppler frequency measured by the central channel and the interferometric phases, $\Delta\theta_H$ and $\Delta\theta_V$, along the two baselines [8]:

$$v_C = -\frac{R_0\Omega_{eff}}{2\pi}\left(\frac{\Delta\theta_H}{d_H}\cos\psi + \frac{\Delta\theta_V}{d_V}\sin\psi\right), \qquad (3)$$

and the Linear Least Square (LLS) estimates $\tilde{\Omega}_{eff}$ and $\tilde{\psi}$ can be found. Further details about the estimation procedure are provided in the Appendix.

The interferometric phase term is a function of the target height, the target-radar geometry and the radar parameters. Zhang et al. [10] studied the effect of the baselines length on the target altitude estimate accuracy: in order to minimise the altitude measurement error, the baselines must be as large as possible. At the same time the range ambiguity must be considered, because the phase difference will be a periodic function with a period of 2π. The height measurement is unambiguous only if:

$$\left|\frac{2\pi h d_i}{\lambda R_0}\right| < \pi\,, \qquad i \in [H, V]\,, \qquad (4)$$

where h is the height measurement, R_0 is the radar-target distance, λ is the central wavelength of the system and d_i is the length of the baselines along the horizontal and vertical directions. The bound of the height measures are given by:

$$-\frac{\lambda R_0}{2d_i} \le h \le \frac{\lambda R_0}{2d_i}\,, \qquad i \in [H, V]\,. \qquad (5)$$

It is clear that there are conflicting requirements on the baselines length d_i: we would like to use long baselines to minimize the effects of the height measurement error, but we also need to keep the baselines length below the ambiguity limits.

The three charts in Fig. 3 represent the ambiguity regions of an hypothetical system at 10 GHz, for different target sizes and a radar-target range of 1 km. The white triangles represent the points in the ambiguity chart where the system is working for different baseline lengths. The illustrated baseline lengths are the same used for the simulation in Section IV.The unambiguous region shrinks when the target gets bigger. To obtain a good 3D image of a big target, it should be very far from the radar and the interferometer baselines should be very short. Fig. 4 presents a similar information, but here there are different plots for different radar-target ranges. The target maximum size is fixed to 25 m. To obtain an unambiguous phase measurement with a 3 m long baseline of such a target, it should stay at 5 km from the radar. These two figures provide valuable insights into how the operational scenario's characteristics can negatively impact the performance of the 3D InISAR system.

A. Multi-Baseline Approaches

Different solutions have been proposed to address the InISAR phase ambiguity by using multiple receivers. More specifically, in [10] two unambiguous antenna pairs are used to estimate the angular motion parameters of the target (measuring-angle antenna set) and other two antenna pairs,

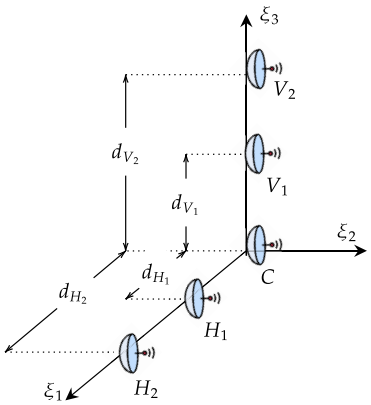

Fig. 5. Multi-baseline 3D InISAR [24].

with longer baselines, are exploited to image the target (imaging antenna set).

In another work [24] a similar geometrical antennas configuration with 5 receivers is used and the ambiguity is addressed by solving a Linear Diophantine Equation (LDE) [25] that allows to obtain the integer ambiguity numbers and unwrap the interferometric phases. The structure of the antennas is depicted in Figure 5. In this paper two different scenarios are analysed: in the first case, the position of the first antennas pair is within the unambiguous limits (Fig. 5, $\overline{H_1C}$ and $\overline{V_1C}$); in the second one, all four receiving antennas are freely placed along the two orthogonal baselines directions. The authors demonstrated that this method yields a substantial improvement in estimation accuracy under high SNR conditions. However, its performance degrades rapidly when the SNR is low due to the numerical sensitivity of the LDE. Ma et al. [26] proposed a solution to mitigate the noise sensitivity of unwrapping methods based on modular arithmetic. They introduced a multi-baseline InISAR system with N antennas, which incorporates a Constant False Alarm Rate (CFAR) detection approach alongside cluster analysis in the ambiguity numbers' space.

The different multi-baseline configurations are effective against the phase wrapping problem and it has been proven that can provide valid three-dimensional reconstructions of the illuminated target. The drawback of these approaches is the near doubling number of antennas (and receiving chains consequently) and the overall increased complexity of the imaging system.

B. Proposed Dual-Frequency Approach

In this study, our approach aims to resolve the phase ambiguity by shifting the diversity from the spatial domain, similar to what multi-baseline systems achieve, to the frequency domain. The main point of a generic multi-channel system is acquiring more interferometric phase measurements of the same underlying geometry. Despite the variations in the measurements due to different baselines or frequencies, all these measurements are related to the same physical object.

This paper will focus on a dual-frequency system. In Figure 6 is sketched the structure of the single receiver: the

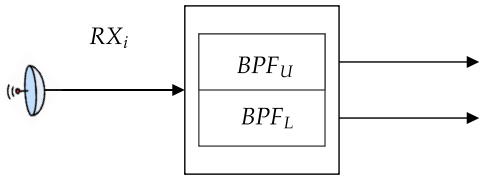

Fig. 6. Generic spatial channel of the interferometer.

bandwidth of the received signal is split into two sub-bands by using two bandpass filters. The subscript U and L mean Upper and Lower. This is done for each spatial channel. This allows us to obtain two interferograms per baseline, one interferogram for each sub-band. Regarding practical implementation, a major attraction of this this approach is that it does not require additional hardware, as it splits the signal following reception. This method is also suitable for re-processing of previously captured data to extract additional information.

Clearly there are some drawbacks associated to the bandwidth splitting. The first one is related to the range resolution loss: by dividing the bandwidth B in half, we are doubling the range resolution ΔR of the system (Eq. 6), because the imaging is being done with the sub-bands (i.e, two images per spatial channel are formed):

$$\Delta R = \frac{c}{2B_i}, \qquad i \in [U, L] \tag{6}$$

where $B_i = B/2$ and c is the speed of light in a vacuum. Subscript index i is omitted from ΔR because the range resolution is the same in both frequency channels. So the overall bandwidth of the system should be wide enough to guarantee a sufficiently fine range resolution after the bandwidth splitting. At the same time, the main bandwidth cannot be too broad, because it would lead to misregistration problems in the following stages of processing. After the sub-bands partition, the scattering centres are extracted from the images. Therefore the images need to be properly aligned, because the same scatterer must be in the same range-Doppler position in both images. The cross-range resolution in the ISAR images is given by:

$$\Delta CR_i = \frac{\lambda_i}{2\Delta\theta}, \qquad i \in [U, L] \tag{7}$$

where $\lambda_i = c/f_i$ is the central wavelength of the i-th channel and $\Delta\theta$ is the total angular variation of the target (i.e., the integration angle in azimuth). If the two central frequencies of the two sub-bands are far apart from each other, the cross-range resolutions ΔCR_i of the images - since it directly depends on the central wavelength (Eq. 7) - will be too different, and it will lead to misregistration errors. In order to better understand what happens by deploying wider bandwidths in terms of image coregistration (as it is shown in 7), and therefore larger relative differences between the two sub-bandwidths, an electromagnetically simulated target is used. This analysis focuses on this kind of target because it offers a more accurate representation of a real object, whereas a point-like target would not deliver comparable insights into the phenomenon (i.e., we would not obtain significant differences between the images coming from upper and lower

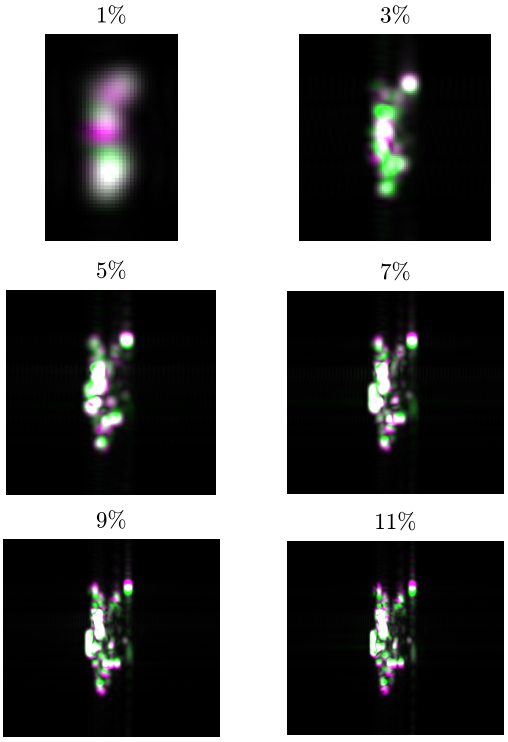

Fig. 7. Pseudo-color representation of the superimposition of the images obtained in the two frequency channels. The images correspond to increment of the relative difference of the central frequencies from 1% to 11%. This comparison highlight the effect of the relative difference of the central frequencies has on the quality of the coregistration.

sub-bands). The data used in this section was simulated by the Air Force Research Laboratory (AFRL) in 2004 by using Xpatch [27] EM scattering code and a CAD model of a backhoe. These data can be requested for free from AFRL Sensor Data Management System (SDMS) website. To quantify the effect of the relative frequency distance between the two channels, two different metrics are used to analyse the differences between the image formed in the upper channel and the image formed in the lower channel. Fig. 8 shows the Mean Square Error (MSE) and the Mutual Information (MI) [28], [29] calculated between the images obtained from upper and lower bandwidths for different values of channels relative distance. By increasing the relative distance, the images start to be significantly different, therefore the MSE increases and the MI decreases. In Fig. 7 this effect is shown visually: each image is the superposition of the ISAR images obtained in the two frequency channels using a pseudo-color representation, with white indicating a good overlap. The image in the upper left corner is generated using a relative difference between the two central frequencies (i.e., the difference normalised w.r.t. the central frequency of the system - 10 GHz in this case) equal to 1% ($B_i = 100$ MHz), while the image in the lower right corner has a relative difference equal to 11% ($B_i = 1.1$ GHz). Where the relative difference is larger, the overlap between the two images decreases and it could lead to errors in the latter stages of processing.

In Fig. 9 the block diagram of the whole processing procedure is illustrated. As introduced before, the full-bandwidth signal coming from each spatial channel is divided into two

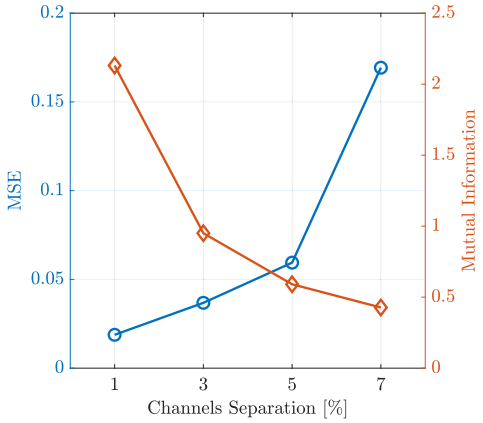

Fig. 8. Mean Square Error and Mutual Information evaluated between the image formed in the upper frequency channel and the image formed in the lower frequency channel.

sub-bands and a range-Doppler (RD) image for each sub-band is formed. The scattering centres are extracted from the upper bandwidth image by using a CLEAN [30] technique, and the position in the RD plane of the extracted scatterers is used to extract the scatterers from the lower sub-band (and this is the reason why a proper registration between the two RD images is critical). This is done for each spatial channel. After the scattering extraction, four different interferograms are formed, two for the vertical baseline and two for the horizontal baseline. The ambiguous interferometric phases and the associated coherence values are then used by the Maximum Likelihood estimator to find the right interferometic phase values for each baseline, the LLS estimates $\tilde{\Omega}_{eff}$ and $\tilde{\psi}$ are calculated (as it is shown in Section II and in the Appendix) and the three-dimensional representation of the target is obtained. In the following section the Maximum Likelihood-based technique used for the phase unwrapping is discussed.

III. Maximum Likelihood Phase Unwrapping

The phase statistic used for the phase unwrapping was obtained for Interferometric SAR applications [31], which implies different underlying statistical assumptions about the observed scene with respect to the ISAR imaging of man-made targets. Despite these differing hypotheses, the core phenomenon of phase wrapping is fundamentally the same in both Interferometric SAR and Interferometric ISAR contexts. This similarity extends to the aspects of decorrelation, such as the effects of Signal-to-Noise Ratio and changes in aspect angles. Therefore the shared underlying phenomena across Interferometric SAR and Interferometric ISAR supports the feasibility of using the same phase statistic model in both scenarios. Eq. 8, as shown at the bottom of the next page, is the probability density function (pdf) of ϕ (the measured phase value) given ϕ_0 (the nominal phase value), with an interferometric coherence value γ, for the single pixel [20]. We can rewrite Equation 8 by using the following relation [8]:

$$\phi_i = \frac{4\pi d}{\lambda_i R_0} h\,, \qquad i \in [U, L] \tag{10}$$

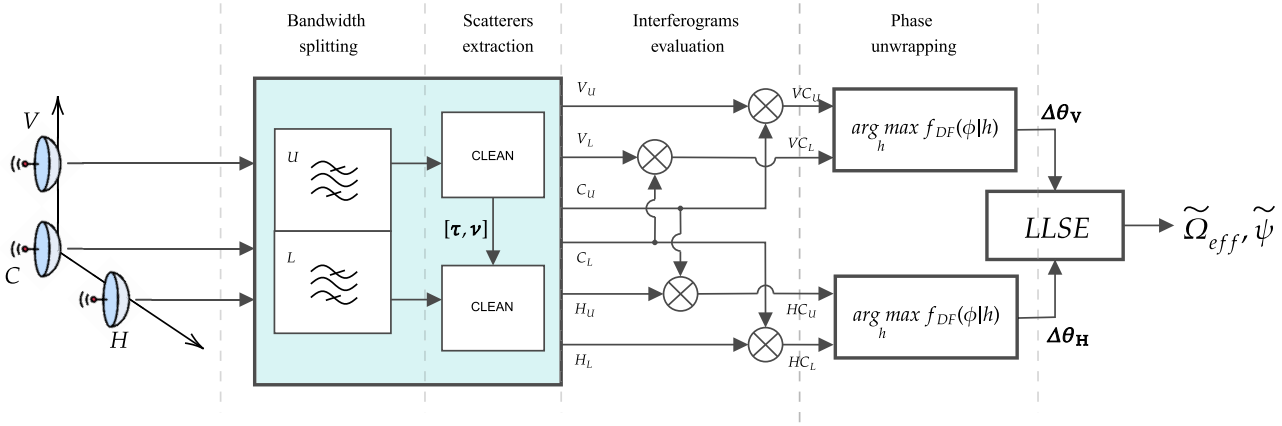

Fig. 9. Block diagram of the system. The vectors $\boldsymbol{\tau}$ and $\boldsymbol{\nu}$ contain the range-Doppler coordinates of the extracted scatterers, while the vectors $\boldsymbol{\Delta\theta_V}$ and $\boldsymbol{\Delta\theta_V}$ are the unwrapped interferometric phases. V, C and H refer to Vertical, Central and Horizontal antennas, U and L stand to Upper and Lower bandwidths. For example: VC_U is the interferogram evaluated between the Vertical and the Central spatial channel, within the Upper bandwidth.

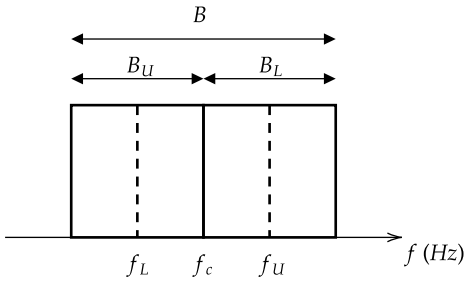

Fig. 10. Frequency representation of the spectrum splitting.

where d is the length of the baseline, λ_i is the wavelength associated to the central frequency of the i-th channel, R_0 is the range of the observed target and h is the height of the scatterer. Therefore, by substituting Eq. 10 in Eq. 8 we obtain Eq. 9, as shown at the bottom of the page. Note that the pdf of Eq. 8 is periodic with 2π, thus Eq. 9 will be periodic too in the height domain. It means the single phase measurement is ambiguous and the real height value cannot be retrieved correctly. In order to solve this ambiguity we need additional and independent phase measurements. To achieve that, the overall bandwidth of the system is splitted in two sub-bandwidths (Fig. 10) and two different interferograms are obtained, one for each frequency channel. Therefore, by having 2 independent phase measurements, where the independence it is satisfied by exploiting nonoverlapping bands [32], the dual-frequency (DF) likelihood function can be written as:

$$f_{DF}(\phi|h) = f_U(\phi|h, \gamma_U, \lambda_U) \cdot f_L(\phi|h, \gamma_L, \lambda_L)\,, \tag{11}$$

where γ_i and λ_i are the coherence and the wavelength for $i \in [U, L]$. The Maximum Likelihood Estimation of the unambiguous height is given by:

$$\hat{h}_{ML} = \arg\max_h f_{DF}(\phi|h). \tag{12}$$

While other choices may be made in terms of splitting the bandwidth, such as overlapping frequency regions, we decided to consider a non-overlapping division in order to obtain two independent processes. Whilst this may not be necessarily the optimal solution, it provides a close form solution that can be readily analysed. Fig. 11 illustrates the principle visually. The probability density functions shown in these plots are derived from two randomly chosen coherence values, γ_U and γ_L, along with a randomly selected height value. The baseline length and frequency values are specified in the figure caption. The right plots display the two marginal probability density functions $f_i(\phi|h, \gamma_i, \lambda_i)$ of the measurements, highlighting the ambiguity caused by the presence of multiple peaks in the probability density functions. The width of the peaks of the pdf is determined by the value of γ (i.e., the uncertainty of the interferometric phase measurement). The lower the γ, the broader the peaks, indicating higher uncertainty. On the left plots, the joint probability density function $f_{DF}(\phi|h)$ is shown, and a distinct maximum can be observed. This maximum corresponds to the maximum likelihood (ML) estimation of the height. One important thing to notice is how the low coherence values can negatively affect the quality of the estimation, by reducing the tapering of the DF likelihood function.

$$f(\phi|\phi_0) = \frac{1}{2\pi}\frac{1-|\gamma|^2}{1-|\gamma|^2\cos^2(\phi-\phi_0)} \cdot \left\{1 + \frac{|\gamma|\cos(\phi-\phi_0)\cos^{-1}\left[-|\gamma|\cos(\phi-\phi_0)\right]}{\sqrt{1-|\gamma|^2\cos^2(\phi-\phi_0)}}\right\} \tag{8}$$

$$f_i(\phi|h,\gamma_i,\lambda_i) = \frac{1}{2\pi}\frac{1-|\gamma_i|^2}{1-|\gamma_i|^2\cos^2\left(\phi-\frac{4\pi d}{\lambda_i R_0}h\right)} \cdot \left\{1 + \frac{|\gamma_i|\cos\left(\phi-\frac{4\pi d}{\lambda_i R_0}h\right)\cos^{-1}\left[-|\gamma_i|\cos\left(\phi-\frac{4\pi d}{\lambda_i R_0}h\right)\right]}{\sqrt{1-|\gamma_i|^2\cos^2\left(\phi-\frac{4\pi d}{\lambda_i R_0}h\right)}}\right\}, \quad i \in [U, L] \tag{9}$$

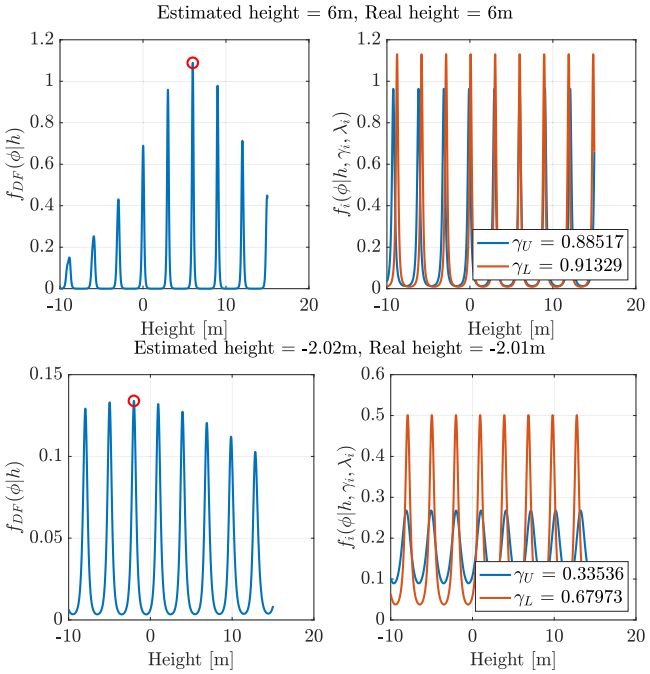

Fig. 11. Example of Maximum Likelihood Estimation of the height of a scatterer @ $d = 5\,m$, $f_U = 10.15\,GHz$, $f_L = 9.85\,GHz$. In the first row, the coherence values are high, thus the peaks are sharper and the resulting dual-frequency probability density function has a strong tapering. In the second row, the peaks are broader and the tapering on the likelihood function is weaker becuase the coherence values are lower. This behavior, if the coherence is really low, leads to wrong height estimations.

In each sub-band interferogram, there exist scatterers that exhibit a frequency coherent behavior. These scatterers, known as frequency-coherent scatterers [33], demonstrate a linear phase variation along the frequency. This information would be very useful to identify and reject scatterers that do not exhibit frequency coherence, thereby enhancing the accuracy of our final results. However, in our specific case, it is challenging to demonstrate this linear behavior since we are utilizing only two sub-bands (i.e., since we have only two points we will always find an exact linear fitting, even if wrapping occurred). This information is still valuable to analyse the performace of the ML-based unwrapping procedure, because it has been observed to fail for some scatterers. This issue is observed in cases where phase wrapping occurs between the two sub-bands, causing a deviation from the expected linear relationship between the phases of scatterers observed at different frequencies. An example is given in Fig. 12 by using the data introduced in Section II-B.

Yet another factor to consider is the limitation associated with the search interval for heights in the ML method. The DF likelihood function will also demonstrate periodic behavior, but with a longer period compared to the single frequency pdf. This implies the need for a reasonable choice of the search interval to prevent the occurrence of multiple peaks. The width of the unambiguous height interval increases as the number of independent phase measurements rises, thereby allowing for a relaxation of constraints on the selection of the height interval by employing a greater number of sub-bandwidths. To accomplish this, maintaining the independence of phase measurements by keeping the sub-bands separate

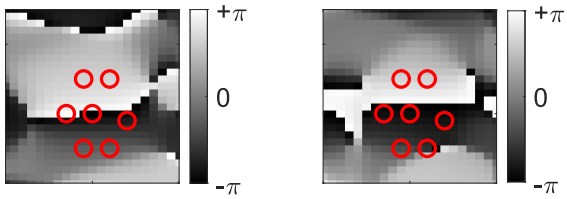

Fig. 12. The two images are two portions of the interferograms evaluated in the two different frequency channels and the red markers identify the positions of the extracted scatterers. By observing the leftmost scatterer it is possible to notice that the phase wraps from one frequency channel to the other. For this scatterer the phase unwrapping will fail.

would require a receiver with a wider bandwidth. If a wider bandwidth receiver cannot be deployed, using smaller sub-bands could be an alternative, although it would further degrade the system's range resolution. This limitation can be addressed by adopting sub-bandwidths that overlap, though this will be the subject of future research.

IV. Point-Like Simulated Target

The simulation is ran 10 times for each baselines length and for each Signal-to-Noise Ratio (SNR) value. The Root Mean Square Error (RMSE) is used as a quality metric in two different ways. The first one is the RMSE evaluated on the reconstruction:

$$\text{RMSE}_{REC} = \sqrt{\frac{1}{M}\sum_{m=1}^{M}\rho_m^2}, \quad \text{with} \tag{13}$$

$$\rho_m = \min_{\boldsymbol{p}_l}\sqrt{\sum\left(\boldsymbol{p}_l - \boldsymbol{p}_m\right)^2} \tag{14}$$

where $\boldsymbol{p}_m$ are the model scatterers positions, $\boldsymbol{p}_l$ are the estimated scatters positions and M is the number of extracted scatterers. For each scatterer of the reconstruction, the closest scatterer from the model is selected and the distance is evaluated. However, relying solely on this measure could potentially lead to misinterpretation of the results. This is because it does not assess the error between the exact pairs of scatterers; rather, it uses the distance to the closest scatterer in the model. Consequently, an incorrect reconstruction might exhibit a RMSE similar to that of a well-reconstructed one, thereby affecting the interpretation of the final outcome.

To further assess the quality of the reconstruction, the RMSE of the LS estimation of the effective rotation vector $\boldsymbol{\Omega}_{eff}$ is used:

$$\text{RMSE}_{LS} = \sqrt{\frac{1}{M}\sum_{m=1}^{M}[Z_m - (bX_m + aY_m)]^2} \tag{15}$$

where all the quantities involved are detailed in Eq. 18 in the Appendix and M is the number of extracted scatterers.

In the RMSEs evaluation we got some outliers, that are usually due to problems that can arise during the scatterers' extraction procedure. Thus only 9 (out of 10) simulation results have been averaged and shown in the following plots. After evaluating the mean value and the standard deviation of all the obtained RMSEs values, the Z-score [34] of the measurements is calculated and the value with the highest Z-score (in absolute value) is discarded. In Table I the parameters of

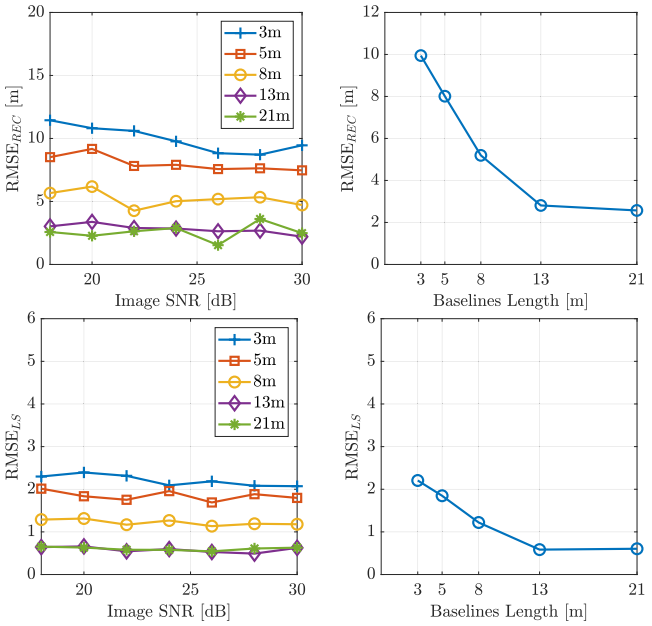

Fig. 13. Dual-frequency results. Left plots: RMSE against the SNR for different baselines lengths. Right plots: RMSE against the baselines length averaged for different SNRs.

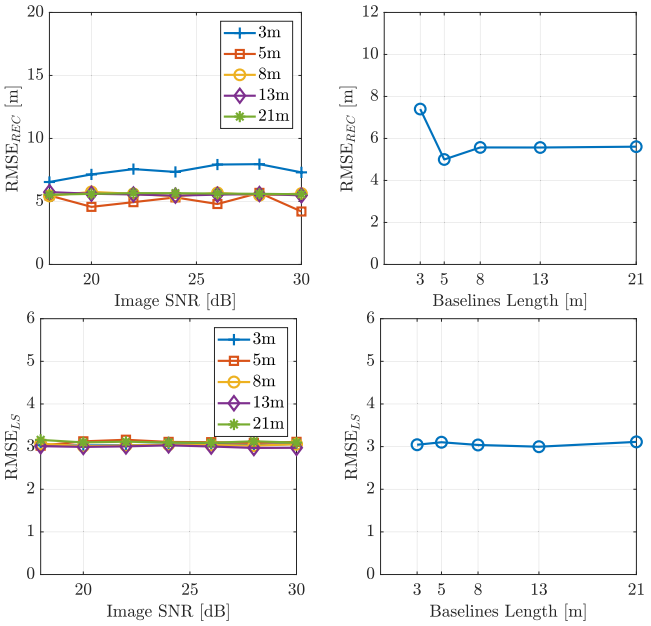

Fig. 14. Single-frequency (ambiguous) results. Left plots: RMSE against the SNR for different baseline lengths. Right plots: RMSE against the baselines length averaged for different SNRs.

TABLE I
PARAMETERS OF THE POINT-LIKE TARGET SIMULATION

Radar parameters	**Values**
Carrier Frequency	10 GHz
Bandwidth	600 MHz
Sub-bandwidth(s)	300 MHz
Upper central Frequency	10.15 GHz
Lower central Frequency	9.85 GHz
No. of transmitted frequencies	256
No. of sweeps	128
Vertical baselines length	$[3, 5, 8, 13, 21]$ m
Horizonal baselines length	$[3, 5, 8, 13, 21]$ m
Polarization	HH
Image SNR	from 18 dB to 30 dB
Target parameters	
Velocity	7 m/s ($\approx$ 13.6 knots)
Range	1000 m
Orientation (roll, pitch, yaw)	$10°, 20°, 60°$

the simulation are detailed. The SNR values are measured in the ISAR images, not on the raw data. The maximum unambiguous baselines length for this scenario is:

$$d_{max} = \frac{\lambda R_0}{2h} = 1.2\,\text{m}\,, \tag{16}$$

where $\lambda = 0.03$ m (carrier frequency $f_c = 10$ GHz), $R_0 = 1000$ m and the maximum target dimension (i.e., its length) $h = 25$ m. Therefore all the baselines length used for the simulation are ambiguous, as previously shown in Fig. 3 and Fig. 4. The single-frequency (SF) system used for the comparison exploit the whole system bandwidth (i.e., 600 MHz).

In Fig. 13 the results for the DF system are plotted. Both RMSE$_{REC}$ and RMSE$_{LS}$ are decreasing for raising values of the SNR and that was predictable; but they are also decreasing for longer baselines length. Increasing the baselines length jointly with a technique to obtain unambiguous phase mesurements improves the final results.

The same does not hold for the ambiguous system. Fig. 14 summarizes the performance of the single-frequency system. The RMSE$_{REC}$ and RMSE$_{LS}$ saturate independently from the SNR value, which is reasonable considering that, whatever the level of the noise is, the system is processing ambiguous phase measurements. The system behaves in a similar way if the analyse the performance against the baselines length.

Fig. 15 and Fig. 16 give a visual confirmation of what is is shown in the previous performance plots. In both figures, subfigures (a) and (c) display the overlay of the target model (marked with red circles) and the reconstructed target (indicated by blue dots). Subfigures (b) and (d) illustrate the two-dimensional least squares (LS) fitting employed to estimate Ω_{eff} and ψ. The metrics presented above each subfigure are computed in accordance with Eq. 14 and Eq. 15. The different axes extent that is obtained on the LS fitting plots are due to the different interferometric phase values obtained in the two cases: in the Single Frequency scenario, the interferometric phases are wrapped, confined within a 2π interval. Conversely, in the Dual Frequency case, these phases are unwrapped, resulting in generally larger absolute values. This distinction accounts for the differing scales observed in the plots. The accuracy of the DF system increases with the length of the baselines, minimising the height mesurement errors. In Tab. II the results of the LS estimation of Ω_{eff} and ψ provide another evidence of the efficiency of the approach. The SNR value of 18 dB marks the point below which we begin to see a noticeable reduction in the system's reconstruction capabilities. It's worth acknowledging the gain that can be attained by deploying of an extended baseline.

Fig. 17 shows the comparison between the average performances of the two approaches, confirming the gain obtained by

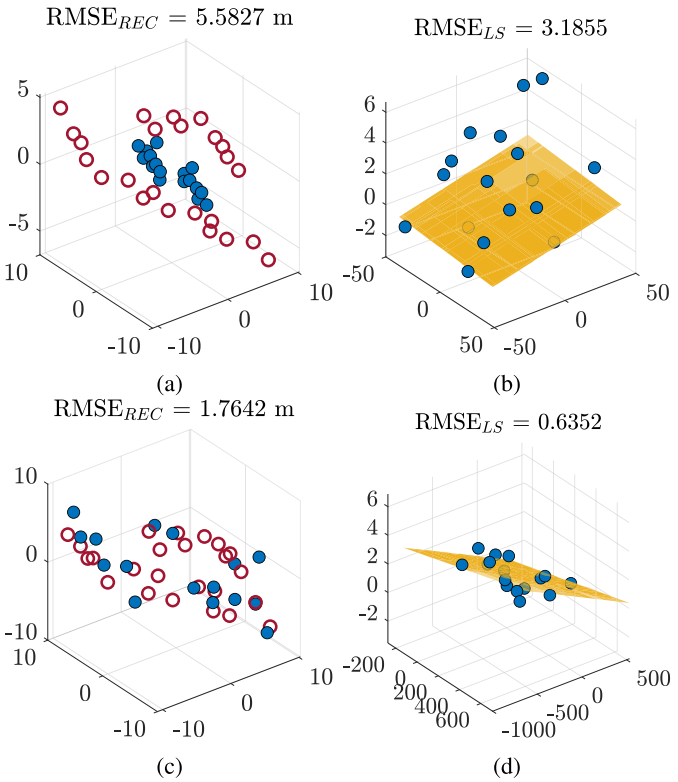

Fig. 15. These results are obtained by using equal baselines of length 21 m and a SNR of 18 dB. Plots (a) and (b) refer to the SF system, while (c) and (d) refer to the DF system. The DF technique can correctly retrieve the effective rotation vector and reconstruct the target.

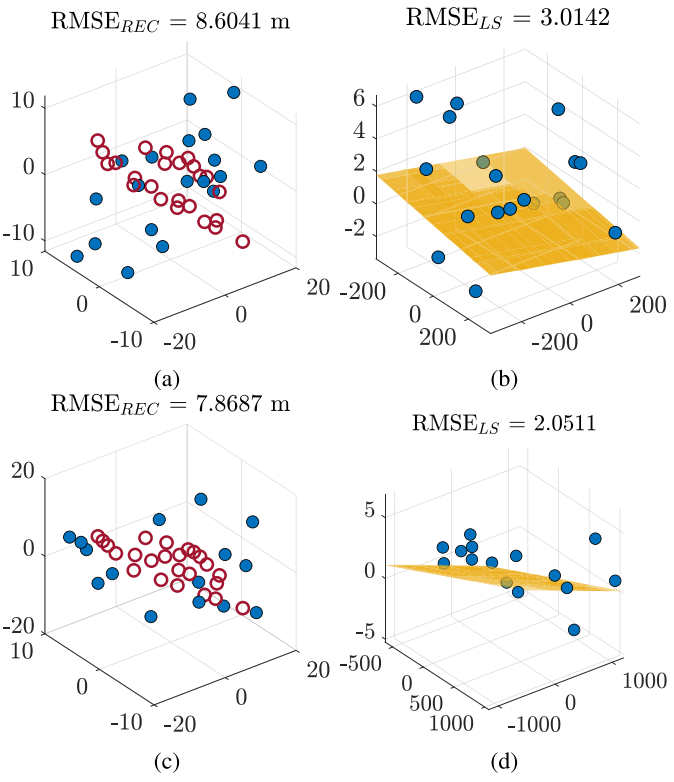

Fig. 16. These results are obtained by using equal baselines of length 3 m and a SNR of 18 dB. Plots (a) and (b) relate to SF, while (c) and (d) correspond to DF. Though reconstructions exhibit marginal distinction, plots (b) and (d) highlight DF's enhanced LS estimation of the effective rotation vector.

TABLE II
COMPARISON OF THE EFFECTIVE ROTATION VECTOR ESTIMATION RESULTS

		$\boldsymbol{\Omega}_{eff}$	ψ
True values		0.0062 rad/s	157.20°
DF	21 m, 18 dB	0.0061 rad/s	139.34°
	3 m, 18 dB	0.0042 rad/s	129.43°
SF	21 m, 18 dB	0.0243 rad/s	−15.67°
	3 m, 18 dB	0.0039 rad/s	−141.11°

using the DF technique. Here the saturation of the RMSE$_{REC}$ and RMSE$_{LS}$ in the single-frequency case is more evident.

This analysis concludes with an examination of how the separation of the central frequencies of channels affects performance, as depicted in Fig. 18. For this evaluation, the relative separation between the two central frequencies ranges from 1% to 7%. The results previously presented were obtained with a relative separation of 3%. The central frequency is equal to 10 GHz. It's important to note that the system's total bandwidth adjusts in response to changes in channel separation. This adjustment is due to the assumption that the receiver's bandwidth is divided equally between the two channels; thus, increasing the separation between the channels correspondingly expands the overall bandwidth. The observed decrease in accuracy at a 1% separation is attributed to the limited range resolution resulting from an overly narrow bandwidth. However, the benefits from longer baselines are still observed. As the frequency separation increases, performance improves

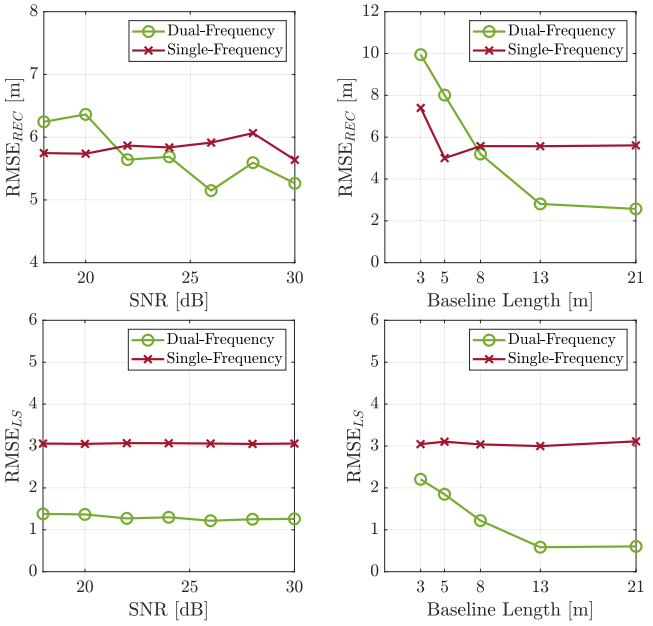

Fig. 17. The SF system is represented by the red curves, while the DF system is denoted by the green curves. The improvement is evident in both metrics, where is possible to appreciate how the usage of the unwrapping technique allows to gain accuracy by deploying longer baselines.

for shorter baselines, but errors begin to rise with longer baselines. Employing a broader frequency spacing enhances the system's sensitivity to interferometric phase variations across frequencies while reducing susceptibility to errors caused

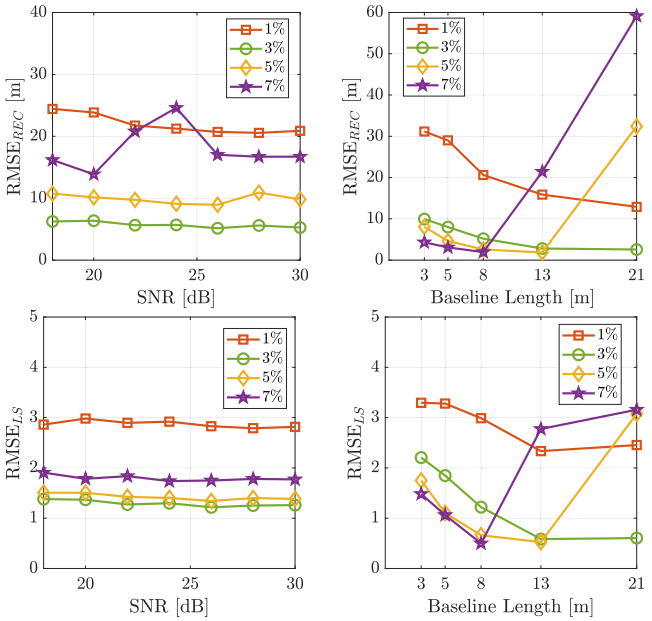

Fig. 18. The first row shows the RMSE obtained on the reconstruction. The second row shows the RMSE of the LS estimation. On the left plots, the curves are obtained by averaging the results for every baselines length. The right plots are obtained by averaging for every SNR.

by interferometric phase standard deviation, thereby yielding an overall performance gain. Furthermore, longer baselines also enhance the system's sensitivity to interferometric phase variations across frequencies, contributing to this performance improvement. The combined effects of broad frequency spacing and extended baselines may lead to the wrapping of interferometric phases across frequencies, a phenomenon we previously encountered in Section III, Fig. 12. Notably, the graph located in the lower right corner of Fig. 18 shows that the error on the LS estimation, tends to 3 for configurations involving wide frequency spacing and long baselines. It is the same saturated value that was obtained while simulating the Single Frequency, ambiguous, system. Given these findings, additional research is necessary to thoroughly examine the constraints and, consequently, the applicability of this method.

V. Conclusion

In this work the problem of the phase unwrapping for 3D-InISAR system is analysed. The proposed approach tries to tackle the ambiguity of the measured phases along the two orthogonal baselines by using two different frequency channels. The obtained results suggest that technique actually improves the quality of the final three-dimensional reconstruction providing unambiguous interferometric phase measurements and harnessing the benefits of utilizing longer baselines.

At the same time, it is crucial to bear in mind the limitations. The primary highlighted concern arises from image misalignment, which depends on the width of the two sub-bands. Another significant aspect to address is about the ability of the system to disambiguate a couple of interferometric phase measurements when they are not consistent along the frequency dimension (i.e., when phase wrapping occurs in the frequency domain). We have shown that increasing both the separation between frequency channels and the length of baselines can lead to ambiguous data. While tight frequency spacing ensures better alignment between the two channels, it may lack the necessary frequency diversity for effective interferometric phase unwrapping. On the other hand, broad frequency spacing achieves greater frequency diversity but at the cost of registration errors and, depending on the geometry, potentially negative impacts on reconstruction quality. This issue will be subject to detailed exploration in upcoming research. Moreover, the quality of the reconstruction can suffer due to the effects of spatial decorrelation when using very long baselines. This aspect is crucial and should not be neglected. It is important to note that this particular issue might not be noticeable when working with simulated point-like targets. This is because the scatterers in such cases are isotropic, and the spatial decorrelation effect does not occur.

A. Future Works

The first future activity will be the application of this method to a real dataset, in order to fully understand the feasibility of the technique in a real scenario. It will also give an insight regarding the effects of the spatial decorrelation.

After that, the research effort will be focused on analysing a multi-frequency system with more than two channels in order to understand if having more phase measurements would help to discern the phase behaviour of a certain scatterer is consistent (i.e., coherent) in frequency. This kind of measurement could also be used for outlier removal and to discard the phase information that would only increase the height reconstruction error.

Another important aspect that will be examinated is the possibility to use overlapped sub-bands, since in this study only non-overlapped bandwidths are used. The MLE approach is based on the assumption of independent phase measurements and this wouldn't be true anymore by using overlapping frequency channels. The advantage of such a configuration would be the use of more frequency channels keeping the overall bandwidth of the system unchanged. Furthermore, it would allow to use larger sub-bands, mitigating the range resolution loss of the system.

Appendix
Effective Rotation Vector LSE

Given the relation between the doppler frequency measured by the central channel and the interferometric phases, $\Delta\theta_H$ and $\Delta\theta_V$, along the two baselines:

$$\nu_C = -\frac{R_0\Omega_{eff}}{2\pi}\left(\frac{\Delta\theta_H}{d_H}\cos\psi + \frac{\Delta\theta_V}{d_V}\sin\psi\right), \qquad (17)$$

we can rewrite it by considering only the m-th scatterer:

$$Z_m = aY_m + bX_m\,, \qquad (18)$$

where $Z = \nu_C$, $Y = -\frac{R_0}{2\pi d_H}\Delta\theta_H$, $X = -\frac{R_0}{2\pi d_V}\Delta\theta_V$, $a = \Omega_{eff}\cos\psi$ and $b = \Omega_{eff}\sin\psi$. Therefore it is possible to estimate Ω_{eff} and ψ by estimating a and b, since Z, Y and X are quantities measured by the system. Here we assume that

the interferometric phases are unambiguous. The estimation is done by calculating the regression plane:

$$\left(\tilde{a}, \tilde{b}\right) = \underset{(a,b)}{\arg\min}\ \Psi(a, b)\,, \tag{19}$$

with

$$\Psi(a, b) = \sum_{m=1}^{M} [Z_m - (aY_m + bX_m)]^2\,, \tag{20}$$

where the subscript m refers to the m-th scatterers extracted from the image and M is the total number of scatterers. Once we derived $\tilde{a}$ and $\tilde{b}$, we can retrieve Ω_{eff} and ψ:

$$\tilde{\Omega}_{eff} = \sqrt{\tilde{a}^2 + \tilde{b}^2}\,, \tag{21}$$

and

$$\tilde{\psi} = \arctan\left(\frac{\tilde{b}}{\tilde{a}}\right). \tag{22}$$

REFERENCES

[1] M. Martorella, F. Salvetti, D. Staglianó, and E. Giusti, "Three-dimensional ISAR imaging: A review," *J. Eng.*, vol. 2019, no. 20, pp. 6823–6828, 2019.

[2] V. Chen and M. Martorella, *Inverse Synthetic Aperture Radar Imaging: Principles, Algorithms and Applications* (Electromagnetics and Radar). U.K.: IET, 2014.

[3] M. Martorella et al., "3D radar imaging for non-cooperative target recognition," in *Proc. 23rd Int. Radar Symp. (IRS)*, Sep. 2022, pp. 300–305.

[4] S. Ghio, E. Giusti, and M. Martorella, "Low-cost database-free automatic target classification using 3D-ISAR," in *Proc. 23rd Int. Radar Symp. (IRS)*, Sep. 2022, pp. 178–183.

[5] J. Cai, M. Martorella, A. Liu, E. Giusti, Z. Huang, and L. Huang, "3D ISAR imaging: ATR based on the alignment between 3D ISAR reconstruction and CAD model," in *Proc. 23rd Int. Radar Symp. (IRS)*, Sep. 2022, pp. 174–177.

[6] C. Y. Pui, B. Ng, L. Rosenberg, and T.-T. Cao, "Target classification for 3D-ISAR using CNNs," *IEEE Trans. Aerosp. Electron. Syst.*, vol. 60, no. 1, pp. 94–105, Feb. 2024, doi: 10.1109/TAES.2023.3271283.

[7] G. Meucci, F. Mancuso, E. Giusti, A. Kumar, S. Ghio, and M. Martorella, "Point cloud transformer (PCT) for 3D-InISAR automatic target recognition," in *Proc. IEEE Radar Conf.*, May 2023, pp. 1–6.

[8] M. Martorella, D. Stagliano, F. Salvetti, and N. Battisti, "3D interferometric ISAR imaging of noncooperative targets," *IEEE Trans. Aerosp. Electron. Syst.*, vol. 50, no. 4, pp. 3102–3114, Oct. 2014.

[9] Q. Zhang and T. Soon Yeo, "Three-dimensional SAR imaging of a ground moving target using the InISAR technique," *IEEE Trans. Geosci. Remote Sens.*, vol. 42, no. 9, pp. 1818–1828, Sep. 2004.

[10] Q. Zhang, T. S. Yeo, G. Du, and S. H. Zhang, "Estimation of three-dimensional motion parameters in interferometric ISAR imaging," *IEEE Trans. Geosci. Remote Sens.*, vol. 42, no. 2, pp. 292–300, Feb. 2004.

[11] E. Giusti, S. Ghio, and M. Martorella, "Drone-based 3D interferometric ISAR imaging," in *Proc. IEEE Radar Conf.*, May 2021, pp. 1–6.

[12] E. Giusti, S. Ghio, and M. Martorella, "Drone-based 3DInISAR: Experimental results," in *Proc. IEEE Radar Conf.*, May 2023, pp. 1–6.

[13] H. Yu, Y. Lan, Z. Yuan, J. Xu, and H. Lee, "Phase unwrapping in InSAR: A review," *IEEE Geosci. Remote Sens. Mag.*, vol. 7, no. 1, pp. 40–58, Mar. 2019.

[14] P. A. Rosen et al., "Synthetic aperture radar interferometry," *Proc. IEEE*, vol. 88, no. 3, pp. 333–382, Mar. 2000.

[15] A. Moreira, P. Prats-Iraola, M. Younis, G. Krieger, I. Hajnsek, and K. P. Papathanassiou, "A tutorial on synthetic aperture radar," *IEEE Geosci. Remote Sens. Mag.*, vol. 1, no. 1, pp. 6–43, Mar. 2013.

[16] W. Xu, E. Chang, L. Kwoh, H. Lim, and W. Cheng, "Phase-unwrapping of SAR interferogram with multi-frequency or multi-baseline," in *Proc. IEEE Int. Geosci. Remote Sens. Symp.*, Aug. 1994, pp. 730–732.

[17] S. N. Madsen and H. A. Zebker, "Automated absolute phase retrieval in across-track interferometry," in *Proc. Int. Geosci. Remote Sens. Symp.*, Jun. 1992, pp. 1582–1584.

[18] S. N. Madsen, H. A. Zebker, and J. Martin, "Topographic mapping using radar interferometry: Processing techniques," *IEEE Trans. Geosci. Remote Sens.*, vol. 31, no. 1, pp. 246–256, Jan. 1993.

[19] S. Li, H. Xu, Y. You, and B. Yang, "Maximum likelihood phase estimation method based on split-spectrum for multi-frequency InSAR system," in *Proc. IEEE Int. Geosci. Remote Sens. Symp.*, Valencia, Spain, Jul. 2018, pp. 2157–2160.

[20] V. Pascazio and G. Schirinzi, "Estimation of terrain elevation by multi-frequency interferometric wide band SAR data," *IEEE Signal Process. Lett.*, vol. 8, no. 1, pp. 7–9, Jan. 2001.

[21] Y. Wang and X. Chen, "3-D interferometric inverse synthetic aperture radar imaging of ship target with complex motion," *IEEE Trans. Geosci. Remote Sens.*, vol. 56, no. 7, pp. 3693–3708, Jul. 2018.

[22] G. Fornaro, G. Franceschetti, and R. Lanari, "Interferometric SAR phase unwrapping using Green's formulation," *IEEE Trans. Geosci. Remote Sens.*, vol. 34, no. 3, pp. 720–727, May 1996.

[23] Z. Yuan, J. Wang, L. Zhao, D. Xiong, and M. Gao, "Phase unwrapping for bistatic InISAR imaging of space targets," *IEEE Trans. Aerosp. Electron. Syst.*, vol. 55, no. 4, pp. 1794–1805, Aug. 2019.

[24] B. W.-H. Ng and H.-T. Tran, "Long-baseline 3D interferometric ISAR," in *Proc. IEEE Radar Conf. (RadarConf)*, May 2017, pp. 0681–0686.

[25] D. Knuth, *The Art of Computer Programming: Seminumerical Algorithms*, vol. 2. Reading, MA, USA: Addison-Wesley, 1997, ch. 4.

[26] M. Ma, G. Qu, S. Liu, Y. Yang, H. Pei, and Q. Chi, "Phase unwrapping based on CFAR detection for multi-baseline InISAR," in *Proc. CIE Int. Conf. Radar (Radar)*, Dec. 2021, pp. 159–162.

[27] D. Andersh et al., "Xpatch 4: The next generation in high frequency electromagnetic modeling and simulation software," in *Proc. Rec. IEEE Int. Radar Conf.*, Jul. 2000, pp. 844–849.

[28] C. Valente and S. T. Wu, "Registration and fusion with mutual information for information-preserved multimodal visualization," in *Proc. Workshop Theses Diss.-Sibgrapi*, 2012, pp. 1–6.

[29] J. Delpiano, "Fast mutual information of two images or signals," in *MATLAB Central File Exchange*. USA: MathWorks, Inc., 2024.

[30] J. Tsao and B. D. Steinberg, "Reduction of sidelobe and speckle artifacts in microwave imaging: The CLEAN technique," *IEEE Trans. Antennas Propag.*, vol. 36, no. 4, pp. 543–556, Apr. 1988.

[31] D. Just and R. Bamler, "Phase statistics of interferograms with applications to synthetic aperture radar," *Appl. Opt.*, vol. 33, no. 20, pp. 4361–4368, 1994.

[32] V. Pascazio and G. Schirinzi, "Multifrequency InSAR height reconstruction through maximum likelihood estimation of local planes parameters," *IEEE Trans. Image Process.*, vol. 11, no. 12, pp. 1478–1489, Dec. 2002.

[33] D. Derauw, A. Orban, and C. Barbier, "Wide band SAR sub-band splitting and inter-band coherence measurements," *Remote Sens. Lett.*, vol. 1, no. 3, pp. 133–140, Sep. 2010.

[34] R. Sprinthall, *Basic Statistical Analysis*. Boston, MA, USA: Allyn & Bacon, 1997.

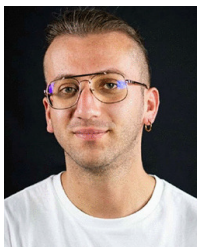

Francesco Mancuso (Graduate Student Member, IEEE) was born in Catanzaro, Italy, in 1994. He received the bachelor's and master's degrees (cum laude) in telecommunication engineering from the University of Pisa, Italy, in 2017 and 2021, respectively, where he is currently pursuing the Ph.D. degree. He is also a Research Collaborator with the CNIT's Radar and Surveillance Systems (RaSS) National Laboratory, Pisa, Italy. Over the past year, he was a Visiting Fellow with Adelaide Radar Research Centre, The University of Adelaide, SA, Australia. His research focuses on radar imaging, radar interferometry, and polarimetric radar. In October 2022, he also received the Professional Qualification (P.Eng.) in Italy. He became a member of Ordine Degli Ingegneri della Provincia di Pisa.

Elisa Giusti (Senior Member, IEEE) received the Laurea (cum laude) and Ph.D. degrees in telecommunication engineering from the University of Pisa, Pisa, Italy, in 2006 and 2010, respectively. From June 2009 to November 2014, she was a Researcher under contract with the Department of Information Engineering, University of Pisa. From November 2014 to December 2015, she was a Researcher under contract with the CNIT-RaSS National Laboratory, Pisa. Since December 2015, she has been a permanent Researcher with the CNIT-RaSS National Laboratory. Since 2009, she has been involved as a Researcher in several international projects funded by Italian ministries (Ministry of Defence and Ministry of Economic Development) and European organizations (EDA and ESA). She is currently the Co-Founder of a radar systems-related spin-off company, ECHOES radar technologies, Pisa. She is the coauthor of more than 80 articles and seven book chapters. She is an Editor of a book titled *Radar Imaging for Maritime Observation* (CRC Press). Her main research interests include radar imaging, including active, passive, bistatic, multistatic, and polarimetric radar. She was a recipient of the 2016 Outstanding Information Research Foundation Book Publication Award for the book *Radar Imaging for Maritime Observation* and Fall 2021 SET Panel Early Career Award (SPECA).

Brian Ng (Member, IEEE) received the B.Sc. degree in mathematics and computer science, the B.E. degree in electrical and electronic engineering, and the Ph.D. degree in electronic engineering from The University of Adelaide, Adelaide, SA, Australia, in 1996, 1997, and 2003, respectively. He is currently an Associate Professor with the School of Electrical and Mechanical Engineering, The University of Adelaide. His research interests include radar signal processing, wavelets, and terahertz (T-ray) signal processing. He is an Associate Editor of IEEE ACCESS and is a regular reviewer of IEEE TRANSACTIONS ON AEROSPACE AND ELECTRONIC SYSTEMS, *IET Radar, Sonar & Navigation*, and international radar conferences. He was a recipient of The University of Adelaide Medal for the top graduate in Electrical and Electronic Engineering. He is an active member of the South Australian Chapter of the IEEE.

Marco Martorella (Fellow, IEEE) received the Laurea (bachelor's and master's) degree in telecommunication engineering and the Ph.D. degree in remote sensing from the University of Pisa, Pisa, Italy, in 1999 and 2003, respectively. He is currently a Professor and the Chair of the RF and Space Sensing Department, University of Birmingham, Birmingham, U.K. He is also the Vice-Director of the CNIT's National Radar and Surveillance Systems Laboratory. He is also the Co-Founder of ECHOES, a radar systems-related spin-off company. He is the author of more than 200 international journals and conference papers, three books, and 17 book chapters. His main research interests include radar, with specific focus on radar imaging, multichannel radar, and space situational awareness. He has presented several tutorials at international radar conferences, has lectured at NATO Lecture Series, and organized international journals special issues on radar imaging topics. He is a member of the IEEE AES Radar Systems Panel and a member of the NATO SET Panel, where he sits as the Co-Chair of the Radio Frequency Technology Focus Group and a member of the EDA Radar Captech. He has chaired several NATO research activities, including three Research Task Groups, one Exploratory Team, and two Specialist Meetings. He was a recipient of the 2008 Italy–Australia Award for young researchers, 2010 Best Reviewer for the IEEE GRSL, IEEE 2013 Fred Nathanson Memorial Radar Award, 2016 Outstanding Information Research Foundation Book Publication Award for the book *Radar Imaging for Maritime Observation*, and 2017 NATO Set Panel Excellence Award.

Open Access funding provided by 'Università di Pisa' within the CRUI CARE Agreement